Check for updates

All-Flexible Artificial Reflex Arc Based on Threshold-Switching Memristor

Depeng Wang, Shufang Zhao, Linlin Li, Lili Wang, Shaowei Cui, Shuo Wang, Zheng Lou,* and Guozhen Shen*

The simulation of human feelings, perceptions, and actions has become an important application field for medical treatment, human–computer interfaces, and intelligent robots. However, the need for various functional units hinders system integration. A threshold-switching memristor is used as the sympathetic nerve center to simulate an unconditioned reflex. High current nonlinearity (10^6) is achieved by adopting a nanocontact structure, and high flexibility (bending radius of ≈5 mm) is obtained by combining the structure with a flexible polymer film. Furthermore, integrating a flexible sensor and a flexible artificial muscle made of ionic polymer–metal composite allows to form an all-flexible complete reflex arc of an unconditioned reflex. The threshold-switching memristor can provide strain-dependent control through simple control logic, indicating the great potential of adopting threshold-switching memristors for primary neuromorphological control and flexible intelligent medical treatment.

1. Introduction

Living organisms can respond to external or internal stimuli due to their highly developed neural control network, which can efficiently receive signals from receptors and activate actuators to respond accordingly. For instance, the reflex arc is controlled by the central nervous system to achieve specific physiological responses involving a few tissues and organs.[1,2]

D. Wang
State Key Laboratory of Automotive Safety and Energy
Tsinghua University
Beijing 100084, P. R. China
D. Wang, S. Zhao, L. Li, L. Wang, Z. Lou, G. Shen
State Key Laboratory for Superlattices and Microstructures
Institute of Semiconductors
Chinese Academy of Sciences
Beijing 100083, China
E-mail: zlou@semi.ac.cn; gzshen@semi.ac.cn
D. Wang, S. Zhao, L. Li, L. Wang, Z. Lou, G. Shen
Center of Materials Science and Optoelectronic Engineering
University of Chinese Academy of Sciences
Beijing 100029, China
S. Cui, S. Wang
Institute of Automation
Chinese Academy of Sciences
Beijing 100190, China

Such responses enable a living organism to operate basic physiological functions with high efficiency, low energy consumption, and stability for adapting to the environment or their self-state. Hence, the design of biological functions and bionic robots has been widely studied in the past few decades.[3–5] However, limitations such as compatibility, toxicity, and complexity limit most bionic systems to applications in industrial and medical auxiliary fields through man–machine control.

Flexible electronics can be compatible with the structural mechanics and engineering functions of living organisms and provide unique advantages for simulating life systems.[6,7] The recent emergence and rapid iteration of flexible bionic neural devices, such as memristors and synaptic transistors, have enabled the advanced design and combinational logic implementation in conventional neural circuits, greatly reducing the complexity of bionic neural circuits.[8–11] In addition, diversified flexible sensors and artificial muscles may endow humans with improved human-level or even super-human-level signal perception and motion control capabilities. Accordingly, by designing an integrated system with multiple flexible devices, many complex applications can be developed, such as artificial prostheses, pain evaluation systems, and humanoid robots.[12,13] However, overly complex systems generally incur high computational complexity and energy consumption of the central processing unit, hindering implementation. Therefore, simple closed-loop systems to complete simple tasks are preferable to implement bionic intervention systems composed of flexible electronics with low computational complexity.

In this work, we combine an MXene/thermoplastic polyurethane (TPU) tensile sensor, an Ag ionic polymer–metal composite (IPMC) actuator, and a novel flexible threshold-switching (TS) device to construct an unconditional reflex arc system. As the operating conditions change, the system can be adjusted through an internal Ag nanowire (NW) pathway. The developed system can simulate a basic reflex arc and perform simple self-control. The system may be used to perform auxiliary functions for treating diseases such as neurogenic bladder dysfunction, as illustrated in this paper. In addition, the adopted approach can help to further clarify the causes of functional failure and provides potential treatment alternatives while potentially providing a practical solution for applications in health monitoring, soft robots, and wearable devices.

2. Results

As shown in **Figure 1**a,b, without control of the midbrain center, urination is a threshold-activated reflex. As the epidermal bladder sensing cells increase in content, the force perception also increases. When the perceived force exceeds a critical value, the pain nerve is activated and transmits signals to the sacral urination center, which in turn triggers the contraction of the detrusor to excrete urine. To develop a fully flexible bionic reflex arc system, we use an MXene/TPU stretch sensor, a TS device obtained by combining Ag NWs and polymer as the nerve center, and an Ag-plated IPMC electrochemical actuator as an artificial muscle. A memristor can serve as a bionic device with resistance transition at a specific voltage threshold, and it can resemble the activation and deactivation of a reflex arc.[10,14,15] Although a remember switch (RS) memristor can maintain a stable memory capacity in resistance, after its activation, it takes a long time or requires a reverse voltage for recovering, increasing the control circuit complexity. On the other hand, a TS device can pass from a high- to a low-resistance state. If the voltage is below a threshold, a resistance transition occurs, quickly recovering the device from a low- to a high-resistance state, as illustrated in Figure 1c. This characteristic can allow artificial nerves to sustain long-term intermittent

work and stability.[16] For operation, we mix high-aspect-ratio ($\approx$300, Figure 1d; Figure S1, Supporting Information) Ag NWs with polyvinylidene fluoride (PVDF) copolymer as variable materials to achieve a high switching ratio and compatibility by flexible and nontoxic characteristics. As a copolymer of PVDF and hexafluoropropylene (HFP) groups, PVDF-HFP has excellent thermal stability, mechanical stability, chemical resistance, and wear resistance, and it can maintain various properties over a long term.

To experimentally compare the TS performance of different PVDF copolymers and Ag-NW-doped dielectric layers, we evaluated PVDF, PVDF-HFP, P(VDF-chlorotrifluoroethylene), and P(VDF-trifluoroethylene). A PVDF–copolymer–DMF (N,N-dimethylformamide) solution with the same mass concentration (20 wt.%) was mixed with the DMF suspension of Ag NWs to obtain four types of polymer and NW suspensions by stirring. As shown in **Figure 2**, we found that the experimental group of PVDF-HFP mixed with Ag NWs provides the highest performance. In the group, when the ratio of Ag NW content to PVDF-HFP solution is 1:1 (volume ratio), the device can realize reversible bidirectional TS. Among the many types of PVDF copolymers, PVDF-HFP has more amorphous domains and better hydrophobic properties than PVDF because of its large constituent groups and poor ferroelectric properties. In
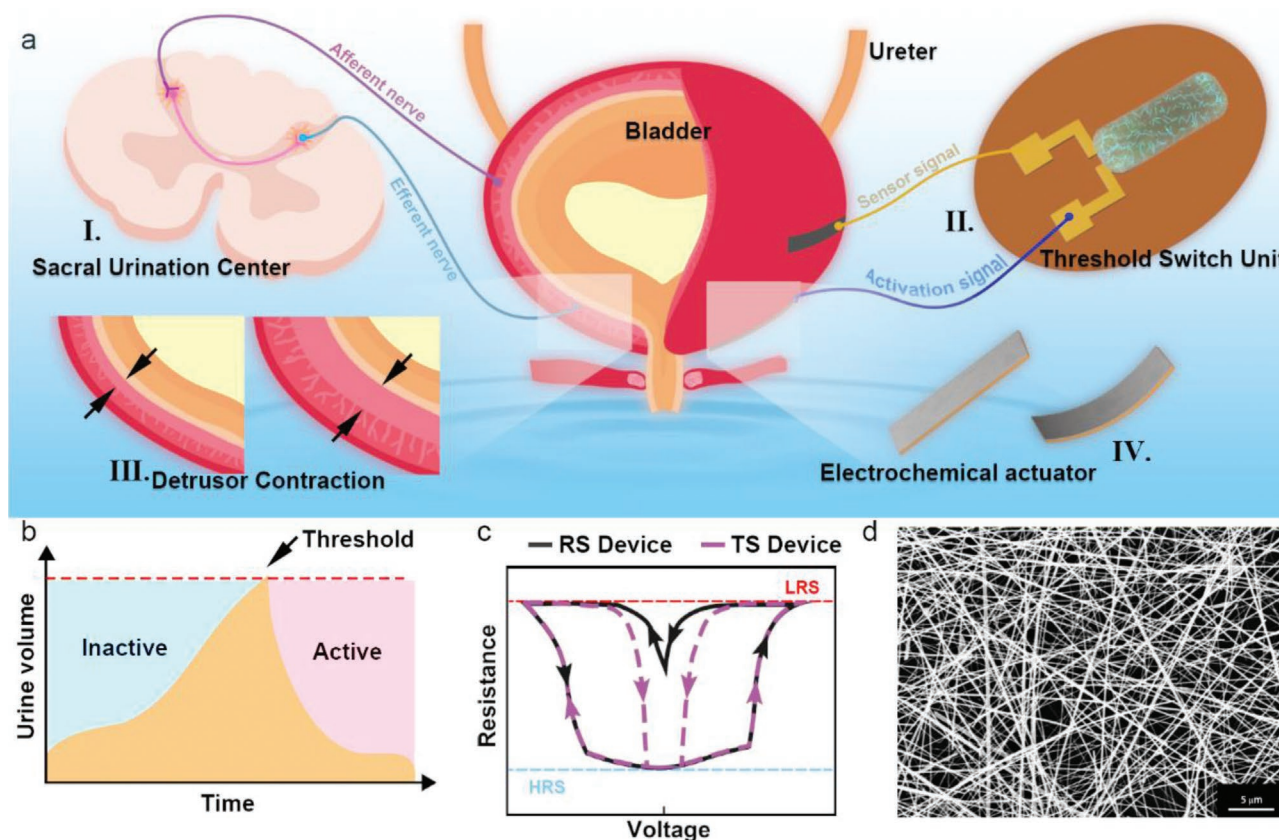
Figure 1. a) Comparison diagram of the biological primary urinary system and artificial urinary system. The bladder surface receptor (stretch sensor) detects the critical pressure response, and the signal is transmitted to sacral spinal cord center (I) (TS device—II). Then, the detrusor muscle (III) (electrochemical actuator is applied—IV) contracts. b) Statistical diagram of urine accumulation and excretion in the bladder. c) Schematic diagram of resistance of RS device and TS devices in response to voltage. d) Scanning electron microscopy image of Ag NWs used in TS memristors.
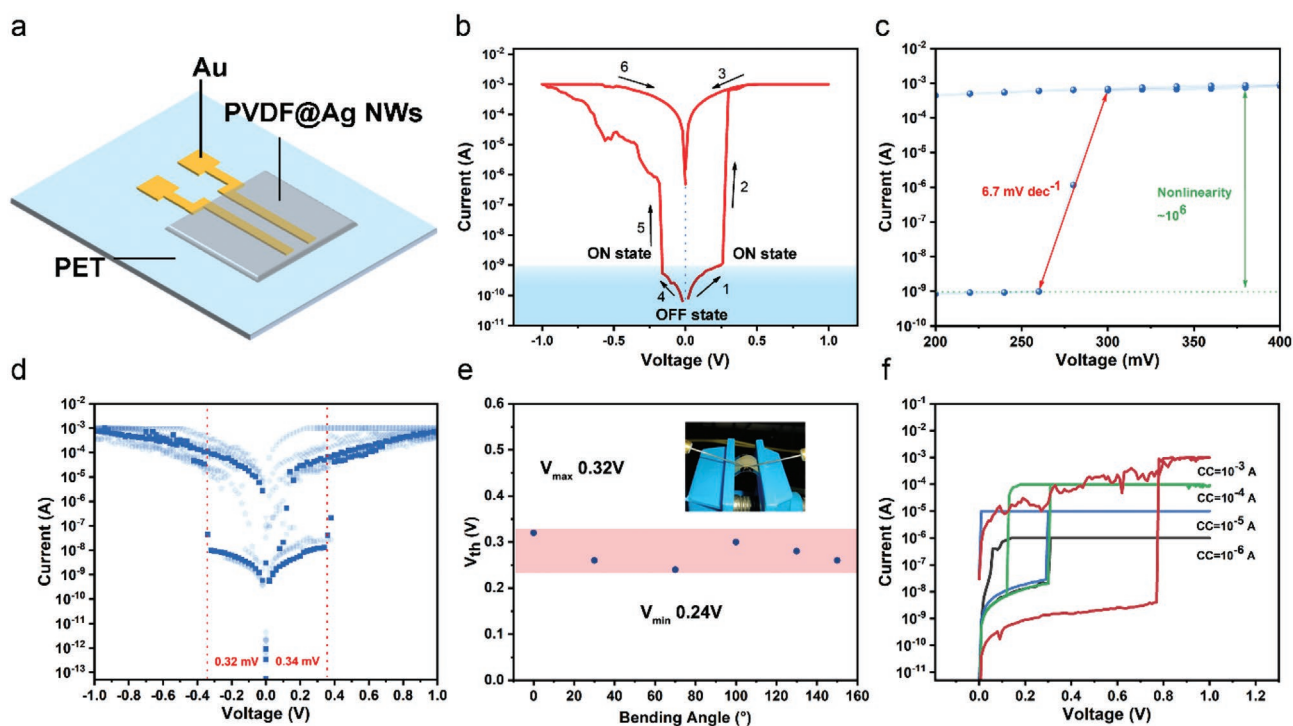
Figure 2. a) Schematic of flexible TS memristor with two-terminal Au/Ag NW–P(VDF-HFP)/Au planar structure. b) Typical I–V characteristics of flexible TS memristor with highly nonlinear, bidirectional, and low-voltage TS behavior. c) Flexible TS memristor with a high nonlinearity of $\approx 10^6$ at V_D of 0.25 V and fast activation slope of 6.7 mV dec^{-1}. d) Ten consecutive cycles of DC voltage sweeps with compliance current of 1 mA showing no deterioration. Positive and negative voltage sweeps were alternately applied. e) Voltage V_{th} according to outward bending angle from 0° to 160°. The inset shows the optical image of the fabricated flexible TS memristor during bending. f) The influence of different compliance current levels on the switch performance of TS memristors.

addition, PVDF-HFP also has the lowest dielectric constant and highest electrical stability among the four evaluated materials.[17] Single nanobelts have been used as resistive materials for TS devices, achieving high switching performance.[16,18] However, the protection characteristics of polymer doping are also important and can be used in flexible electronic devices for complex operating environments. Owing to the protection of PVDF-HFP, the deterioration reaction of external water and oxygen is avoided, and a long working life of Ag-NW TS devices can be achieved.

The flexible TS memristor is fabricated using a nanocontact strategy.[19] The memristor comprises two planar Au/Cr electrodes sandwiching a transparent thin film including Ag NWs diffused in the P(VDF-HFP) copolymer (Figure 2a, optical image is shown in Figure S2, Supporting Information). This simple structure provides bidirectional TS in a flexible device. Figure 2b shows the typical TS behavior of the Ag NW TS memristor under a forming voltage of ≈ 1 V. The initial resistance is high until it abruptly switches from the OFF state (10^{-10} A) to the ON stage (10^{-3} A) at activation voltage V_{ON} of ≈ 0.25 V. Then, as the voltage returns to zero, the flexible TS memristor almost immediately returns to the OFF state, differing from the RS device with a slow behavior. Symmetry endows the flexible TS memristors with bidirectional switching, as reported in a previous study.[6] The nonlinear area is magnified in Figure 2c, and nonlinearity reaches above 10^6 at V_{ON} of 0.25 V. The steep slope is almost 6.7 mV dec^{-1}, being similar to that of other flexible switching devices.

Uniformity, speed, and stability of implementation are also important for applying flexible TS devices. Figure 2d shows ten circle I–V curves obtained continuously when a single flexible TS memristor was operated in DC mode. Voltage threshold V_{th} and other characteristics do not show degradation, indicating the device reliability, which was also verified under bending conditions. The threshold voltage does not change dramatically with an increase in external bending (>0), as shown in Figure 2e, which depicts the relation between threshold voltage and bending angle. Interestingly, activation current I_{ON} decreases when the bending angle increases, implying that a large bending angle reduces the elastic tensile deformation and internal Ag NW density, weakening the nanocontact.

We established four experiment groups of compliance current ranging from 10^{-6} to 10^{-3} A to test the highest current in the ON state. At the first switching in DC mode, as shown in Figure 2f, voltage V_{th} (0.8 V) at a compliance current of 10^{-3} A is far higher than that of the other groups (0.25 V). At the initial formation of the effective link in the conductive filament, Ag atoms connected to the positive pole in the PVDF-HFP film are fused by Joule heat to change the initial shape and gradually drift under the electric field and try to form an electrical connection. Thus, the device requires a high voltage and produces a large switching ratio to establish a connection for the first time. After the voltage returns to zero, the Ag NW path breaks under the action of interface free energy and external perturbation. However, the broken fragments remain near the path,

**ADVANCED
SCIENCE NEWS**

www.advancedsciencenews.com

**ADVANCED
FUNCTIONAL
MATERIALS**

www.afm-journal.de

and the subsequent conductive connections do not require long atomic drifts, substantially reducing the threshold voltage compared with that required for the first activation.

The environment composed of dielectric materials in which the nano-conducting materials are located is crucial for the formation of conductive filaments. The structure of alternating C−F bonds and C−H bonds formed by highly electronegative fluorine atoms in PVDF materials makes the polymer have higher polarity and larger intramolecular dipole moment. Therefore, the conductive filaments are greatly hindered by the dielectric material in the process of forming and breaking. To validate the PVDF copolymer, we evaluated other PVDF copolymers as dielectrics and performed the same I–V characteristic test (Figure S3, Supporting Information). Scanning electron microscopy images show a randomly oriented Ag NW network embedded in the surface layer of the PVDF polymer (Figure S4, Supporting Information). Among PVDF-HFP, due to the larger molecular groups and less polarity, a better balance can be achieved after mixing with silver nanowires. It can not only induce the internal generation of conductive paths by voltage, but also delay the breaking speed of conductive paths by utilizing high chemical stability and residual polarity. Through a reasonable ratio of similar polar groups and nanowire concentrations, the electrical properties of threshold switching devices can be effectively regulated, such as the magnitude of the turn-on voltage and the speed of recovery after turning off. Hence, NW-based TS memristors should have a suitable protective layer material with electrical and chemical stability. We also tested the infrared absorption spectra of PVDF-HFP monomer and PVDF-HFP mixed with silver NWs (Figure S5, Supporting Information). The pair of absorption bands at 1170 is mainly caused by the CF_2 stretching vibration. The sharp absorption of 1070 is the vibration of the crystalline phase, the absorption bands at 875, 835 are the characteristic absorption of the amorphous phase, and the 1400 absorption band is the variable-angle vibration of CH_2.[20] The results show two positions of the absorption peaks of the control group remain the same, but the absorption intensity is different, which may be caused by the difference in concentration caused by the silver NWs supporting the polymer grid.

As mentioned above, the device switches back to the high-resistance state automatically as the voltage returns to zero, indicating the rupture of unstable filaments. To clarify the underlying mechanism, we developed the phenomenological model shown in **Figure 3**a for the proposed flexible TS memristor. The Ag NWs randomly dispersed in P(VDF-HFP) do not form an effective conductive path. Before the voltage gradually increases to the threshold voltage, Ag atoms from the Ag NWs are oxidized to Ag^+ ions ($Ag - e^- \rightarrow Ag^+$). Along the electric field, the positively charged ions move toward Ag NWs nearby and are reduced back to Ag atoms ($Ag^+ + e^- \rightarrow Ag$). The junction of Ag filaments is produced according to the accumulation of Ag atoms, and the flexible TS memristor is activated. When the voltage drops back to zero, owing to Rayleigh instability and Joule heat, the Ag NW pathway breaks at the most vulnerable position and stays near the pathway, such that the memristor returns to the OFF state.[21]

Owing to the irregular Brownian motion, the Ag atoms remaining in the channel gradually move away from the current position.[22,23] However, continuous voltage switching causes a large number of Ag atoms to gather along the pathway and enlarge the current path, which is also reflected in the increased OFF-state current. According to Figure 3b, the continuous cycle causes the switch current ratio to decrease rapidly. When controlling the voltage stimulation interval, as shown in Figure 3c, both the threshold voltage and OFF-state current gradually recover to their initial state. Compared with TS memristors developed in recent years,[18,19,24–30] the proposed flexible TS memristors have a high switching ratio and ultralow operating voltage, enabling low energy consumption (Figure 3d).
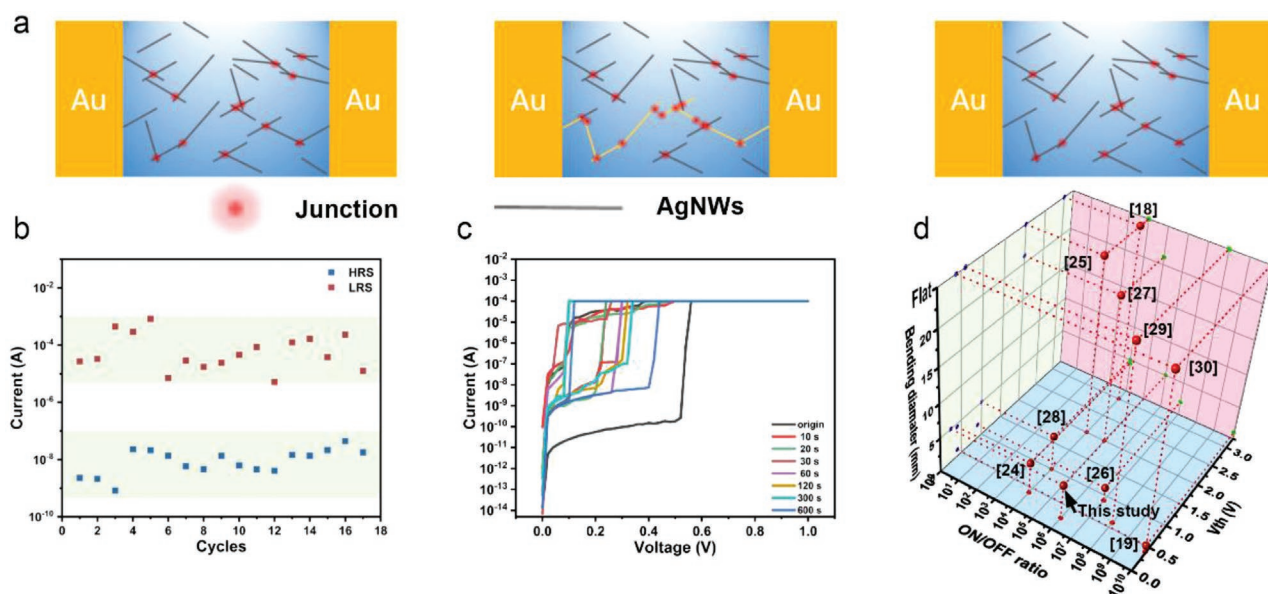

Figure 3. a) Schematic of flexible TS memristor switching between OFF and ON states. The yellow path represents the conductive filament formed by adjacent Ag NWs. b) Variation of current in ON and OFF states under continuous cycle test. c) I–V characteristics of flexible TS memristors at different cycle intervals. d) Statistical diagram of ON/OFF ratio, threshold voltage, and bending radius of planar TS devices.

Considering the variation in the high-resistance state of TS memristors after multiple adjacent activation cycles, we speculate that such variation resembles synapses with certain memory capabilities. To verify the strengthened connection and its maintenance to establish artificial synaptic devices, multiple sets of spike stimulation experiments were conducted and analyzed considering the spike voltage and reading voltage. As shown in **Figure 4**a, under stimulation using a single spike with a reading voltage of 0.001 V and a spike voltage of 1 V, the TS memristor rapidly increases its current from 1.17×10^{-9} to 1.36×10^{-3} A, showing a large variation (1.16×10^6). By comparing the resistance states of the TS devices before and after threshold switching (at the same read voltage), we define a value "RVS" whose resistance varies with the state to quantify the static effect of the pulse on the strength of the weighted connection. RVS is obtained by taking the rate number of the resistivity after the change/the resistivity before the change

$$\text{RVS} = \frac{R_{\text{After}}}{R_{\text{Before}}} \tag{1}$$

After removing the spike stimulation, the current drops and remains at $\approx 10^{-6}$ A. Compared with the initial current, the spike stimulation increases the conductivity of the TS memristor,
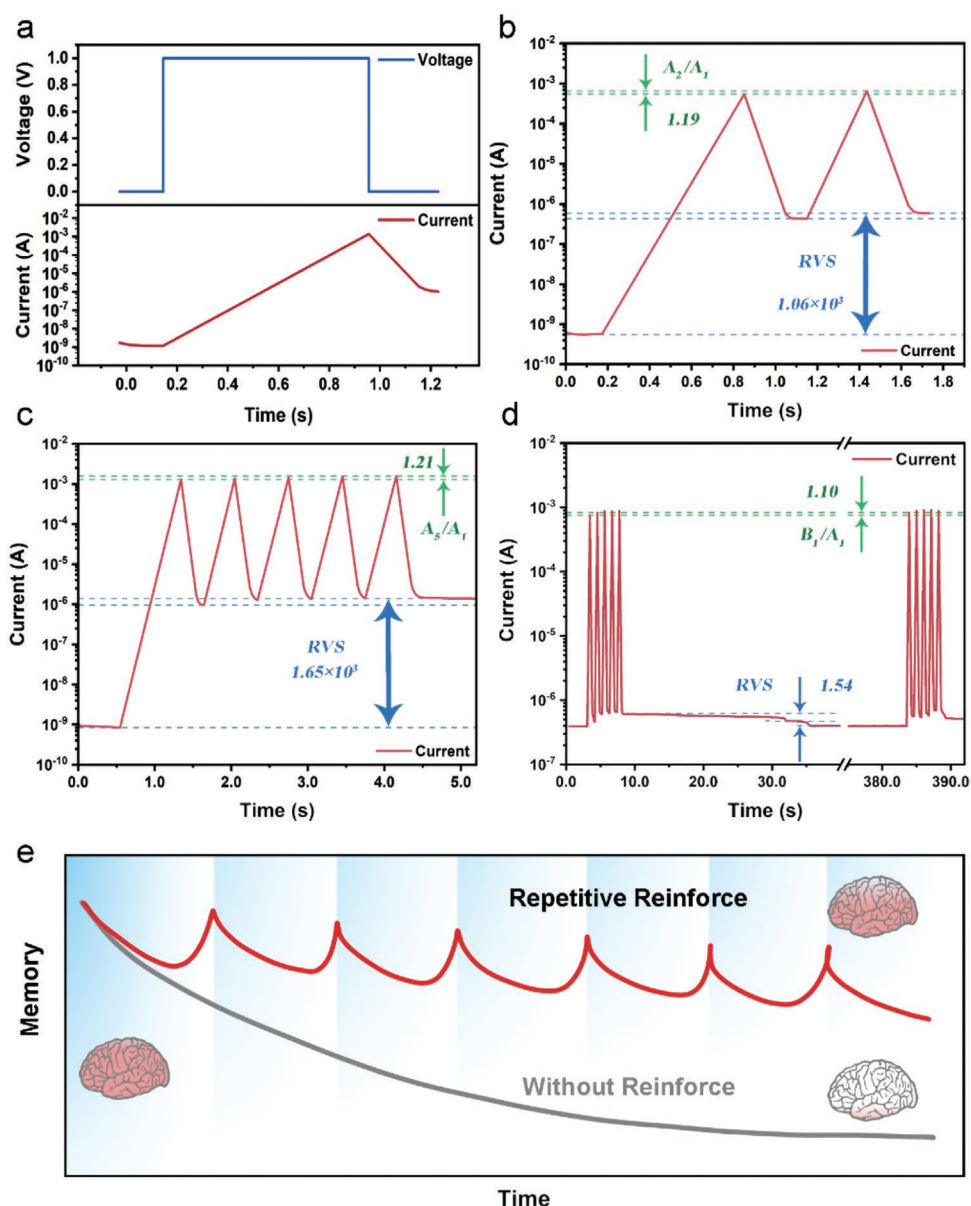
Figure 4. a) Current response of TS memristor under single-spike stimulation with spike voltage of 1 V and reading voltage of 0.001 V. b) Under the stimulation of two adjacent spikes, the current of the TS memristor exhibits paired-pulse facilitation ($A_2/A_1 \sim 1.19$) while maintaining a high RVS (1.06×10^3) under reading voltage of 0.001 V. c) Under the stimulation of five adjacent spikes, the current of the TS memristor exhibits paired-pulse facilitation ($A_5/A_1 \sim 1.21$) while maintaining a high RVS (1.65×10^3). d) Two groups of spike stimuli were applied to TS memristor with an interval of 6 min between groups to resemble learning. e) Ebbinghaus forgetting curve.

ADVANCED
SCIENCE NEWS
www.advancedsciencenews.com

ADVANCED
FUNCTIONAL
MATERIALS
www.afm-journal.de

indicating a memory capacity similar to the formation of synapses. The TS memristor was further subjected to five consecutive spikes with a reading voltage of 0.001 V and spike voltage of 1 V, obtaining the results shown in Figure 4b,c. Obviously, we found from the double-pulse stimulation that the pulse current of the latter part is higher than the former part, and its double-pulse alienation rate (A_2/A_1) is 1.19. As the number of pulses increases, the internal conductance connection strength of the TS memristor gradually increases. Compared with double pulse alienation, the alienation rate A_5/A_1 of five pulses is 1.21, In addition, continuous spike stimulation has a negligible effect on the ON-state current of the TS memristor. Moreover, the current under the reading voltage shows a substantial increase of 60% compared with the reading-voltage current under double-spike stimulation. The change in reading-voltage current is caused by the continuous spike stimulation, which increases the strength of the conductance inside the TS memristor. Accordingly, the resistance variation of the TS memristor composed of PVDF-HFP and Ag NWs indicates temporal memory of external stimuli, which can be strengthened by continuous stimulation.

To evaluate the resistance maintenance characteristics (i.e., memory characteristics) of the TS memristor over time, we applied two groups of spike stimulations with an interval of 6 min to the TS memristor and conducted a "learning–forgetting–learning" test. The ratio of first peak current B_1 in the second group to first peak current A_1 in the first group is 1.1 (Figure 4d). In addition, the reading voltage shows that the conductivity strength increases after the first set of spike stimulation and returns to its initial state after 30 s. As Figure 4d is consistent with Figure 3c, increasing spike stimulation of the TS memristor increases its reading-voltage current. However, as the interval between stimulation groups increases, the connection strength gradually decreases until restoring the initial high-resistance state. Therefore, voltage stimulation with suitable interval control allows to maintain the TS memristor active continuously. The memory characteristics are similar to the manifestation of the Ebbinghaus forgetting curve (Figure 4e).[31] For some repetitive reflexes, such as the pain reflex, multiple high-response stress reflexes induce organisms to adjust their perception thresholds of the pain reflex arc to avoid excessive damage and elicit the reflex sooner in subsequent exposures to the triggering stimulus. The function of modulating the reflex threshold is the basis for biological self-adjustment and self-evolution under external stimuli.

To imitate a low-level reflex arc, we used three devices for sensing, control, and motion, integrating a system to elicit a basic reflex.[32,33] TiC, a 2D MXene material with excellent electrical conductivity, was coated on the TPU film obtained by electrospinning to prepare a highly sensitive stretch sensor.[34,35] A schematic diagram of the device simulation stretching biosensor and its photograph are shown in **Figure 5**a. As shown in Figure 5b and Figure S6 (Supporting Information), the stretch range of the MXene/TPU stretch sensor ranges from 10% to 40%, which is similar to the bladder radius expansion rate (volume change rate of 300%), and the maximum stretch strain response can reach 225%. As the Ag NW TS system is used as the control unit, and a considerable voltage shift is needed to activate the mechanism, a large voltage change should be

applied. As a result, the sensor must react to the degree of stretching with a broad range of resistance adjustments. Therefore, MXene was selected as the sensitive sheet. Given the interconnected TiC content, the tensile sensor has an apparent reaction under limited stress because of the excellent conductivity of this 2D material, and the laminated construction causes the relative change rate of the instrument to increase drastically under high pressure owing to the interconnections. The non-conductivity of the nanocomposite is caused by separation under high pressure (Further detail in Figure S7, Supporting Information). As shown in Figure 5b, when the maximum effective stretch reaches 40%, the relative resistance change rate is as high as 525.62, and the maximum gauge factor is 1314.05. In addition, we measured the real-time relative resistivity of the stretch sensor according to the loading/unloading strain, and the results show no obvious hysteresis during loading (95 ms) and unloading (385 ms) (Figure 5c). Then, in Figure S8 (Supporting Information), we further checked the unidirectional I–V characteristics under different stretching degrees and found that the sensor has high stability and linearity. We also performed a 5 Hz frequency tensile response loop test on the device, and the results are presented in Figure S9 (Supporting Information).

IPMC, a kind of electrochemical actuator based on a Nafion film, was used as an artificial muscle (Figure 5d). Owing to their large deformation and operational stability in the air, they are promising candidates for artificial muscles. In addition, the low working voltage (2–3 V) also complies with the working range of the proposed system, being easy to integrate with other equipment and possibly preventing biological damage in applications.[36] When a specific voltage is applied to both sides, the prepared actuator strip exhibits a large bending deformation, and the degree of bending can be determined by varying the applied voltage bias (Figure 5e; Figure S10, Supporting Information). Owing to the capacitor structure, the I–V curve of the actuator presents the electrochemical characteristics of a double-layer supercapacitor (Figure S11, Supporting Information). We chose Nafion N117 film as the substrate, and prepared dense silver layers on both sides of it as electrodes by electrochemical plating. The detailed SEM characterization diagram is shown in Figure S12 (Supporting Information). When the actuator is subjected to cyclic voltammetry tests at different rates, the device also exhibits an obvious charging curve similar to that of a supercapacitor (Figure S13, Supporting Information). The actuator withstands ten cycles of periodic voltage switching between 3 and −3 V, demonstrating its reversibility and reliability (Figure 5f).

By integrating the three devices, we conducted a biological unconditioned reflex test on the obtained system. We considered the bladder diastolic reflex using the MXene/TPU stretch sensor as the afferent nerve and the NW-based TS memristor as the parasympathetic nerve to control the muscles, which were simulated by the IPMC actuator to complete the artificial reflex arc.[12] The appearance of the bladder changes according to the amount of stored urine. When urine enters the bladder, the bladder wall stretches until it is full and is flattened by the overlying bowel into an oval shape.[37,38] The stretch sensor was glued to the periphery of the artificial bladder represented by a similarly shaped balloon, and the parallel TS memristor was placed on top with a small change (Figure 5g). As the balloon
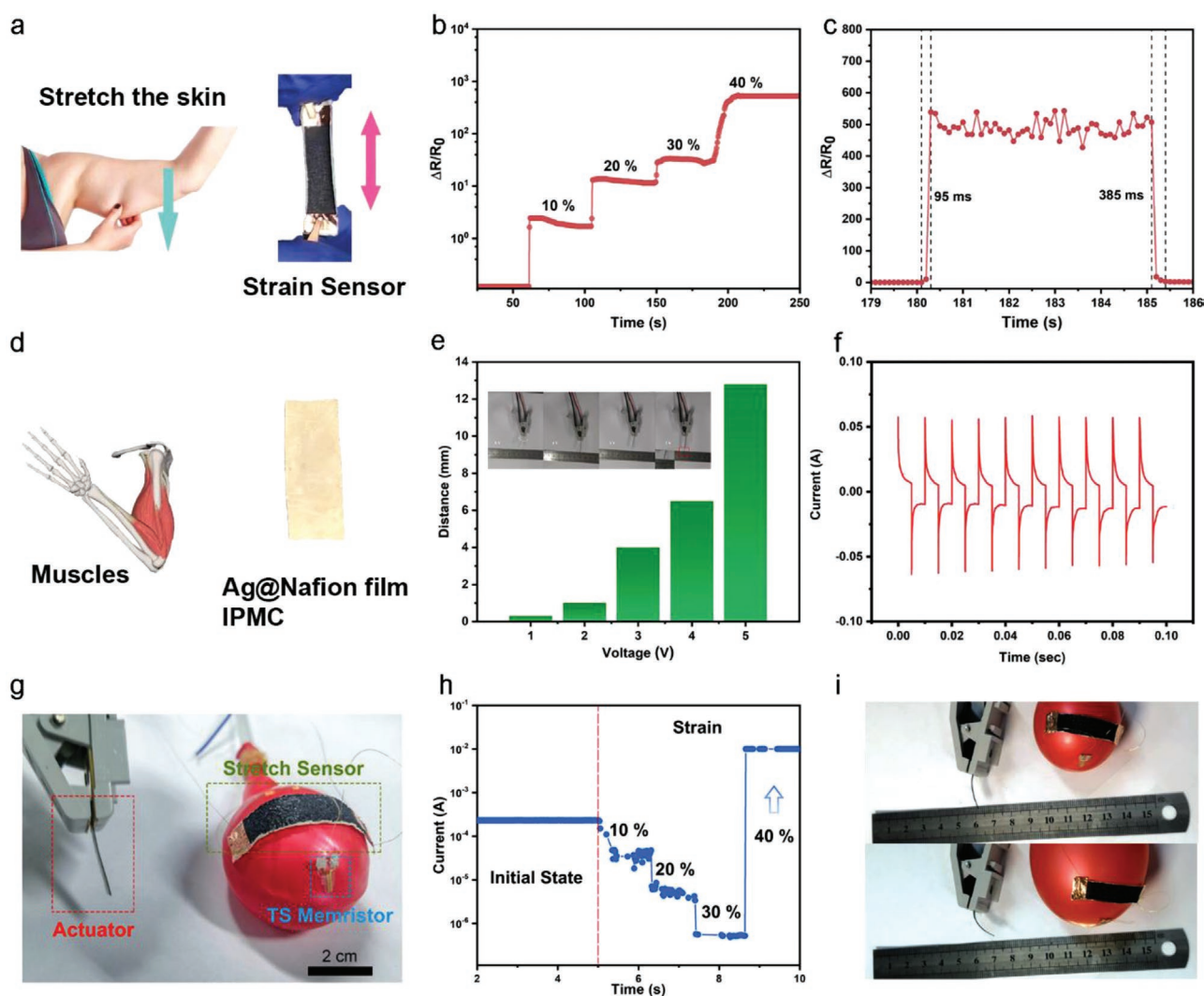
Figure 5. a) Human skin stretching and stretch sensor photographs. b) Current curves over time of MXene/TPU stretch sensor at different stretching levels. From 10% to 40%, the relative resistance of the stretch sensor increases step by step, indicating that the sensor can identify different stretching degrees over a reasonable range. c) Response time and recovery time of MXene/TPU stretch sensor. d) Schematic of human muscle and photograph of Ag-Nafion IPMC film. e) Tip-to-tip displacement bar graph of Ag-IPMC actuator measured at DC voltages from 1 to 5 V. f) The working current curve of IPMC under the stimulation of positive and negative 3 V square wave voltage g) Optical picture of the complete system combined with a balloon. h) Current curve over time of control circuit during stretching test. i) Displacement of Ag-IPMC actuator before and after system response.

is filled with liquid and begins to expand, the sensor stretches. Through the parallel connection of the two devices, strain-dependent programming of the resistance of the TS memristor is achieved. Given that the reference resistor is known, the initial low strength of the tensile sensor shields the parallel TS memristor, and the voltage is insufficient to activate the TS memristor, with the total current remaining at 10^{-4} A. As the stretch sensor is further stretched, the total resistance and voltage of the parallel circuit increase, but the TS memristor cannot be activated below the threshold voltage. The diastolic reflex of a biological bladder is activated after reaching a stimulation threshold, forcing the detrusor to initiate urination. As shown in Figure 5h, the developed system changes sharply from a high-resistance to a low-resistance state only when the strain stimulus reaches the preset threshold (Figure 5i; Movie S1, Supporting Information). Simultaneously, given the

self-recovery of the TS memristor, when the tensile sensor signal drops below the threshold, the shielded TS memristor gradually recovers from the low-resistance to the high-resistance state without requiring a reverse voltage.

The proposed system may be applicable for medical assistance to extend the simulation of the bladder relaxation reflex. In many neurogenic bladder dysfunctions, such as detrusor underactivity or underactive bladder, a reduced contraction strength often leads to excessive urination time or incomplete urination. Currently, intermittent urinary catheterization by inserting a straw into the urethra is considered the most effective method for emptying the bladder. However, this method increases the susceptibility to urinary tract infections, and its use is limited by periodic pain. Without requiring intubation, the proposed system may be used to monitor changes in the bladder volume and perform urination assistance.

3. Conclusion

The electrical and neurological properties of Ag NWs and P(VDF-HFP) composite dielectric materials used as threshold transition memristors were investigated in this study. An artificial device was developed to replicate the action of the diastolic reflex arc in a biological bladder. The continuous stretch signal was successfully transformed into a control signal following the all-or-none rule, and an electrochemical actuator was activated for reflex control owing to the threshold modulation of a stretch sensor and an Ag NW TS memristor. By using nanocontacts, we found that various factors influence the transition of the Ag NW network TS memristor, including the concentration and length of Ag NWs as well as the electrical stability of the dielectric content, which are essential for operation. NW-based TS memristors have high application potential owing to their simple preparation, versatile modulation constraints, and electrical self-recovery characteristics. Furthermore, the system developed in this study, which was made of modular electronic components, can be used in flexible electronics applications such as wearable electronics, alternate neural prostheses, and intelligent flexible robots.

4. Experimental Section

Synthesis of Ag NWs: Poly(vinylpyrrolidone) (0.2 g) was added to 25 mL of ethylene glycol and mixed until full dissolution at 60 °C. The solution was then filled with 0.25 g $AgNO_3$ and 3.5 g $FeCl_3$ until dissolved completely by stirring. The mixed solution was transferred immediately to a reaction bowl and heated to 130 °C for 5 h in an oven. After the hydrothermal reaction, the vial was centrifuged twice at 3500 rpm for 5 min with acetone and ethanol. The obtained Ag NWs were scattered in DMF. Finally, the solution was concentrated at 0.8 g mL^{-1}.

Fabrication of Flexible TS Memristor: First, a polyethylene terephthalate substrate was ultrasonically cleaned with deionized water and then ultrasonically cleaned with ethanol and toluene. Next, Au (50 nm)/ Cr (5 nm) symmetric electrodes (W/L = 500) were deposited on the substrate by photolithography. Then, the NW suspension was mixed with the DMF solution (0.2 g mL^{-1}) of P(VDF-HFP) and stirred for 1 h to obtain a mixed solution of Ag NWs-P(VDF-HFP). Finally, a flexible printed device (Prtronic Tech) was used to coat the mixed solution on the electrodeposition and dried at 40 °C.

Fabrication of Ag-IPMC Actuator: Before IPMC was manufactured, Nafion N117 membranes were treated by being roughened with sandpaper, immersed in a 5 wt.% H_2O_2 aqueous solution, boiled for 30 min, washed repeatedly in deionized water, and boiled at 100 °C for 1 h. Then, the resulting film was immersed in 0.1 mol L^{-1} H_2SO_4 and boiled for 30 min. The film was boiled again in deionized water at 100 °C for 1 h for full swelling. The metal Ag electrode layer was prepared on the Nafion membrane by assisted electroless plating. This process included 1) immersing the treated Nafion membrane in a 0.25 mol L^{-1} NaOH solution, keeping it at 25 °C for 40 min, and then placing it in a 0.03 mol L^{-1} Ag(NH$_3$)OH aqueous solution for 15 h. 2) Then, 0.025 mol L^{-1} $C_6H_{12}O_6$ solution was added dropwise to the reaction solution and stirred slowly. The Ag ammonia ions adsorbed on the surface of the Nafion membrane were reduced to metallic Ag and nano-adsorbed on the Nafion membrane. 3) The obtained membrane was washed with distilled water and ultrasonicated for 5 s to eliminate the influence of bad Ag particles. To ensure conductivity of the Ag electrode, electroless plating steps 1–3 were repeated twice. The Nafion membrane with a high-quality Pt electrode was dried at 90 °C for 4 h and then reswelled in deionized water to eliminate solvent impurities in the Nafion membrane.

Fabrication of MXene/TPU Stretch Sensor: Four grams of TPU was added to 16 g of DMF, and the solution was stirred and dissolved in an oil bath at 60 °C to obtain a colorless, transparent solution. Then, the solution was inserted into a syringe, and the TPU film was spun at 12 kV and 15 cm between the nozzle and collection plate. Finally, the TPU film was cleaned using a plasma machine (12 W), and an aqueous MXene solution was drip-coated on the pre-stretched film and air-dried at room temperature to obtain the stretch sensor.

Measurements: The electrical and sensing characteristics were measured using a Keithley 4200 SCS station and a Keysight 1500A analyzer. For pressure sensing, voltage pulses were delivered by a function signal generator (Keithley 2182A) to obtain electrical signals with different pulse widths/intervals/frequencies. The external pressure was delivered by a fixed mass weight.

Supporting Information

Supporting Information is available from the Wiley Online Library or from the author.

Acknowledgements

Conflict of Interest

The authors declare no conflict of interest.

Data Availability Statement

The data that support the findings of this study are available from the corresponding author upon reasonable request.

Keywords

[1] A. Cully, J. Clune, D. Tarapore, J.-B. Mouret, *Nature* **2015**, *521*, 503.

[2] R. Merindol, A. Walther, *Chem. Soc. Rev.* **2017**, *46*, 5588.

[3] L. Osborn, R. Kaliki, A. Soares, N. Thakor, *IEEE Trans. Haptics* **2016**, *9*, 196.

[4] W. Hu, G. Z. Lum, M. Mastrangeli, M. Sitti, *Nature* **2018**, *554*, 81.

[5] M. Wehner, R. L. Truby, D. J. Fitzgerald, B. Mosadegh, G. M. Whitesides, J. A. Lewis, R. J. Wood, *Nature* **2016**, *536*, 451.

[6] B. Zhong, L. Wang, K. Jiang, G. Shen, *Adv. Sci.* **2022**, *9*, 2103257.

[7] L. Li, D. Wang, D. Zhang, W. Ran, Y. Yan, Z. Li, L. Wang, G. Shen, *Adv. Funct. Mater.* **2021**, *31*, 2104782.

[8] S. F. Cogan, *Annu. Rev. Biomed. Eng.* **2008**, *10*, 275.

[9] K. Tybrandt, D. Khodagholy, B. Dielacher, F. Stauffer, A. F. Renz, G. Buzsaki, J. Voros, *Adv. Mater.* **2018**, *30*, 1706520.

[10] Z. Wu, J. Lu, T. Shi, X. Zhao, X. Zhang, Y. Yang, F. Wu, Y. Li, Q. Liu, M. Liu, *Adv. Mater.* **2020**, *32*, 2004398.

[11] S. Choi, J. Yang, G. Wang, *Adv. Mater.* **2020**, *32*, 51.

[12] K. He, Y. Liu, M. Wang, G. Chen, Y. Jiang, J. Yu, C. Wan, D. Qi, M. Xiao, W. R. Leow, H. Yang, M. Antonietti, X. Chen, *Adv. Mater.* **2020**, *32*, 1905399.

[13] Y. Kim, A. Chortos, W. T. Xu, Y. X. Liu, J. Y. Oh, D. Son, J. Kang, A. M. Foudeh, C. X. Zhu, Y. Lee, S. M. Niu, J. Liu, R. Pfattner, Z. N. Bao, T. W. Lee, *Science* **2018**, *360*, 998.

[14] M. Prezioso, F. Merrikh-Bayat, B. D. Hoskins, G. C. Adam, K. K. Likharev, D. B. Strukov, *Nature* **2015**, *521*, 61.

[15] H. G. Manning, F. Niosi, C. G. da Rocha, A. T. Bellew, C. O'Callaghan, S. Biswas, P. F. Flowers, B. J. Wiley, J. D. Holmes, M. S. Ferreira, J. J. Boland, *Nat. Commun.* **2018**, *9*, 3219.

[16] M. Xiao, D. Shen, K. P. Musselman, W. W. Duley, Y. N. Zhou, *Nanoscale* **2018**, *10*, 6069.

[17] J. C. Barbosa, J. P. Dias, S. Lanceros-Mendez, C. M. Costa, *Membranes* **2018**, *8*, 3.

[18] M. Xiao, D. Shen, M. H. Futscher, B. Ehrler, K. P. Musselman, W. W. Duley, Y. N. Zhou, *Adv. Electron. Mater.* **2019**, *6*, 1900595.

[19] M. Wang, W. Wang, W. R. Leow, C. Wan, G. Chen, Y. Zeng, J. Yu, Y. Liu, P. Cai, H. Wang, D. Ielmini, X. Chen, *Adv. Mater.* **2018**, *30*, 1802516.

[20] U. R. Farooqui, A. L. Ahmad, N. A. Hamid, *Polym. Test.* **2017**, *60*, 124.

[21] Z. Wang, M. Rao, R. Midya, S. Joshi, H. Jiang, P. Lin, W. Song, S. Asapu, Y. Zhuo, C. Li, H. Wu, Q. Xia, J. J. Yang, *Adv. Funct. Mater.* **2017**, *28*, 1704862.

[22] T. Wan, Y. Pan, H. Du, B. Qu, J. Yi, D. Chu, *ACS Appl. Mater. Interfaces* **2018**, *10*, 2716.

[23] N. Fata, S. Mishra, Y. Xue, Y. Wang, J. Hicks, A. Ural, *J. Appl. Phys.* **2020**, *128*, 124301.

[24] J. Ge, S. Zhang, Z. Liu, Z. Xie, S. Pan, *Nanoscale* **2019**, *11*, 6591.

[25] W. Lee, J. Park, S. Kim, J. Woo, J. Shin, G. Choi, S. Park, D. Lee, E. Cha, B. H. Lee, H. Hwang, *ACS Nano* **2012**, *6*, 8166.

[26] J. Sun, H. Wang, F. Song, Z. Wang, B. Dang, M. Yang, H. Gao, X. Ma, Y. Hao, *Small* **2018**, *14*, 27.

[27] W.-J. Sun, Y.-Y. Zhao, X.-F. Cheng, J.-H. He, J.-M. Lu, *ACS Appl. Mater. Interfaces* **2020**, *12*, 9865.

[28] Y. Song, G. Feng, C. Sun, Q. Liang, L. Wu, X. Yu, S. Lei, W. Hu, *Chem. - Eur. J.* **2021**, *27*, 13605.

[29] S. Kim, J. H. Son, S. H. Lee, B. K. You, K. I. Park, H. K. Lee, M. Byun, K. J. Lee, *Adv. Mater.* **2014**, *26*, 7480.

[30] R. Midya, Z. Wang, J. Zhang, S. E. Savel'ev, C. Li, M. Rao, M. H. Jang, S. Joshi, H. Jiang, P. Lin, K. Norris, N. Ge, Q. Wu, M. Barnell, Z. Li, H. L. Xin, R. S. Williams, Q. Xia, J. J. Yang, *Adv. Mater.* **2017**, *29*, 1604457.

[31] D. G. Roe, S. Kim, Y. Y. Choi, H. Woo, M. S. Kang, Y. J. Song, J. H. Ahn, Y. Lee, J. H. Cho, *Adv. Mater.* **2021**, *33*, 2007782.

[32] F. A. Hassani, W. Y. X. Peh, G. G. L. Gammad, R. P. Mogan, T. K. Ng, T. L. C. Kuo, L. G. Ng, P. Luu, S. C. Yen, C. Lee, *Adv. Sci.* **2017**, *4*, 1700143.

[33] Z. Gao, S. Chen, R. Li, Z. Lou, W. Han, K. Jiang, F. Qu, G. Shen, *Nano Energy* **2021**, *86*, 106078.

[34] X. Jin, L. Li, S. Zhao, X. Li, K. Jiang, L. Wang, G. Shen, *ACS Nano* **2021**, *15*, 18385.

[35] D. Wang, L. Wang, Z. Lou, Y. Zheng, K. Wang, L. Zhao, W. Han, K. Jiang, G. Shen, *Nano Energy* **2020**, *78*, 105252.

[36] D. K. Biswal, D. Bandopadhya, S. K. Dwivedy, *Int. J. Precis. Eng. Manuf.* **2012**, *13*, 777.

[37] A. Parekh, A. D. Cigan, S. Wognum, R. L. Heise, M. B. Chancellor, M. S. Sacks, *J. Biomech.* **2010**, *43*, 1708.

[38] S. Hannah, P. Brige, A. Ravichandran, M. Ramuz, *ACS Omega* **2019**, *4*, 1907.